Supporting Information for "Low-volatility vapors and new particle formation over the Southern Ocean during the Antarctic Circumnavigation Expedition"

Andrea Baccarini[1,2], Josef Dommen[2], Katrianne Lehtipalo[3,4], Silvia Henning[5], Robin L. Modini[2], Martin Gysel-Beer[2], Urs Baltensperger[2]and Julia Schmale[1]

[1]School of Architecture, Civil and Environmental Engineering, École Polytechnique Fédérale de Lausanne, Lausanne, Switzerland

[2]Laboratory of Atmospheric Chemistry, Paul Scherrer Institute, Villigen PSI, Switzerland

[3]Institute for Atmospheric and Earth System Research/Physics, University of Helsinki, Helsinki, Finland

[4]Finnish Meteorological Institute, Helsinki, Finland

[5]Institute for Tropospheric Research, Experimental Aerosol and Cloud Microphysics, Leipzig, Germany

Contents of this file

Introduction

This supporting information contains first a text section describing the operation and calibration of a nitrate chemical ionization Atmospheric Pressure Interface Time-of-Flight Mass Spectrometer (CI-APi-ToF)(Jokinen et al., 2012). A second text

section describes how the extended Aerosol Inorganic Model (E-AIM; http://www.aim.env.uea.ac.uk/aim/aim.php, last access: 22 April 2021) (S. L. Clegg & Seinfeld, 2006) was used to model the gas-particle partitioning of methanesulfonic acid (MSA) using an aerosol mixture representative of the Southern Ocean aerosol.

Figures S1 to S13 provide additional information to the results shown in the main text and are referenced therein, whereas Figures S14 and S15 are related to Text S1 and S2. Tables S1 and S2 are related to Text S2 and provide details regarding the E-AIM simulation.

Text S1. Nitrate CIMS operation and calibration

Sulfuric acid, MSA and iodic acid were measured with a nitrate CIMS (Jokinen et al., 2012). These molecules are detected either as clustered with the nitrate monomer or as deprotonated species. The concentration of a species X is calculated as:

$$[X] = C \frac{\mathrm{X^-} + \mathrm{XNO_3^-}}{\sum_{n=0}^{2} (\mathrm{HNO_3})_\mathrm{n}\mathrm{NO_3^-}}, \quad (1)$$

with X- being the deprotonated species and C the calibration factor which can be experimentally determined. The instrument is typically calibrated by injecting a known amount of sulfuric acid which can be produced in different ways, for this work we used a series of experiments at the PSI smog chamber (SC). The sensitivity of the instrument can be assumed to be constant (*i.e.* the same calibration factor C can be applied), under the assumption that each collision leads to a stable cluster. This is the case for sulfuric acid, MSA and iodic acid because they have a lower proton affinity than nitric acid (Jokinen et al., 2012; Eisele & Tanner, 1993; Sipilä et al., 2016).

The CI inlet is generally operated with an electric field driving the nitrate ions inside the sample flow. However, for a part of ACE no voltage was applied to the inlet due to a

technical issue. In this case, diffusion and turbulence in the inlet drive the mixing of the nitrate with the sample flow. A different sensitivity could be expected compared to a CI inlet operated in the standard way. However, as shown below, the difference was found to be smaller than the calibration uncertainty. Therefore, the same calibration constant was used for the entire ACE campaign.

The calibration of the nitrate CIMS was performed at the PSI SC, a $27m^3$ flexible Teflon bag inside a wooden enclosure where temperature can be controlled. Four xenon arc lamps and a set of 80 UV-A light tubes are used to initiate photochemistry inside the chamber, further details on the chamber can be found in Paulsen et al. (2005). Experiments were carried out injecting SO_2 at a mixing ratio between 0 and 15 ppb, ozone between 0 and 250 ppb and trimethylbenzene (TMB) between 0 and 10 ppb. The temperature inside the chamber was kept fixed at $20 \pm 2\,°C$ and the RH was varied between 20% and 40%. The reaction of SO_2 with OH was used to produce sulfuric acid, whose concentration inside the chamber can be described by a simple kinetic model:

$$\frac{d[H_2SO_4]}{dt} = k_{OH\,+\,SO_2}[OH][SO_2] - (W + CS)[H_2SO_4], \tag{2}$$

with $k_{OH\,+\,SO_2}$ being the reaction rate constant (Wine et al., 1984), W the sulfuric acid wall loss rate inside the chamber and CS the condensation sink. The wall loss rate was estimated to be $(3.5 \pm 0.9) \times 10^{-3}$ s^{-1}. The CS represents the sulfuric acid loss term to the particles and can be calculated from the particle number size distribution following Dal Maso et al. (2002).

Equation 2 can be used to calculate the concentration of sulfuric acid inside the chamber at the steady state as:

$$[H_2SO_4] = \frac{k_{OH\,+\,SO_2}[OH][SO_2]}{W + CS}. \tag{3}$$

The OH concentration is estimated from the decay of TMB which reacts with it at a known reaction rate constant (Kramp & Paulson, 1998).

The calibration result is reported in Figure S14, where the ordinate shows the sulfuric acid concentration calculated from Equation 3 and the abscissa the average of the measured sulfuric acid signal normalized by the reagent ion concentration. The uncertainty of the calculated sulfuric acid concentration was obtained by standard error propagation from Equation 3, whereas the uncertainty on the CI-APi-ToF measurements was calculated as the standard error of the mean. A weighted least squares regression was applied to estimate the calibration constant C as described in Equation 1. The CI inlet is usually operated with an electric field to force the reagent ions into the sample flow. During the calibration the instrument was run also without the electric field in order to simulate the CI-APi-ToF operating conditions during ACE. The results presented in Figure S14 clearly show that there is no systematic difference between the two operating modes of the inlet. Therefore a single calibration value was used:

$$C_{ACE} = 6.9 \times 10^9 [-50\% + 100\%] \text{ molecule cm}^{-3}, \quad (4)$$

where the calibration coefficient was already corrected for diffusional losses of sulfuric acid in the inlet line. An uncertainty of $[-50\% + 100\%]$ was associated with the calibration factor, which is a standard estimate for sulfuric acid measurements in the field. This estimate is larger than the linear regression confidence interval and accounts for the intrinsic variability of field conditions, which are difficult to quantify.

Text S2. E-AIM calculation

E-AIM was used to estimate MSA partitioning over the Southern Ocean aerosol. MSA is not included among the default species available in the E-AIM library and needs to

be created by the user defining some of its fundamental thermodynamic properties. A part from the most basic properties, such as the molar mass and the molar volume, MSA thermodynamic properties are not readily available and model studies often use very different values. Table S1 reports all the values that were used in this study and the corresponding references, as a general criterion we decided to use values based on experimental results rather than modelling or ab initio calculation. By reporting all the information required to include MSA in E-AIM we hope to provide a useful reference for the community and to foster discussion, which thermodynamic properties are the most appropriate values for MSA.. All the values in Table S1 were taken directly from the cited reference with minimal adaption (*e.g.* unit of measure), with the only exception of the surface tension parameters. In this case we had to recreate the surface tension data from Myhre, D'Anna, Nicolaisen, and Nielsen (2004) and fit them with the function defined by Dutcher, Wexler, and Clegg (2010) to obtain the parameters in the form required by E-AIM.

Concerning the specific details of the E-AIM simulations, we fixed the temperature to 273.15 K and varied relative humidity (RH) between 60% and 100%. These are representative values for the environmental conditions encountered during the two transects described in the main text. E-AIM model II was used for the simulations containing only sulfate, ammonium and MSA whereas E-AIM model IV was used when also sodium and chloride were included. Aerosol components were forced to stay in the liquid form as the efflorescence RH is below typical values encountered in the marine boundary layer. However, E-AIM model IV is unable to account for supersaturated solutions, for this reason only RH values above $\sim 75\%$ could be considered when using this model.

The aerosol composition used for the E-AIM simulation was based on ion chromatography (IC) analysis of daily PM_{10} filters. These filters were collected using a high-volume sampler on the upper deck of the ship. The sampler had an automatic system to stop the sample flow when the wind was coming from the direction of the ship chimney. However, this system proved to be not sufficient to prevent sampling of the exhaust plume as evident from the high elemental carbon (EC) concentrations measured on some of the filters (larger than $1\,\mu g\ m^{-3}$). We used EC as a proxy for contamination from the ship exhaust on the PM_{10} filters because ambient concentration of black carbon in the Southern Ocean is generally very low (less than 40 ng m^{-3})(Schmale et al., 2019). Figure S15 shows the ammonium and the non-sea-salt (nss) sulfate concentrations measured on the PM_{10} filters as a function of EC, there is an evident positive correlation indicating that both ammonium and nss-sulfate are probably affected by the ship exhaust. However, nss-sulfate and ammonium seem to become independent from the ship exhaust for EC values below about $0.6 - 0.7\,\mu g\ m^{-3}$. Under this condition, the concentration of these two compounds is dominated by natural sources and not by the ship exhaust. Hence, we decided to consider only the filters characterized by an EC concentration below $0.65\,\mu g\ m^{-3}$ to minimize the influence of the ship exhaust. Additionally, we also excluded the filters with a total sampled volume below 240 m^3, which is one third of the maximum possible volume. Such a low sampling volume indicates that the samplers were often turned off because of the wind coming from the direction of the ship chimney. Figure S5 shows the concentration of the ions relevant for the E-AIM calculation from this filter selection.

In order to understand the effect of aerosol composition on MSA partitioning we run three different sets of simulations using E-AIM. For the first set of simulations we decided

to fix the nss-sulfate concentration based on the median concentration measured during ACE and varied the ammonium concentration to obtain different ratios (2 : 1, 1 : 1 and 1 : 2). The MSA concentration was fixed based on the median MSA to nss-sulfate ratio (Fig.S5). Figure S6 shows the model predictions in terms of the MSA vapour pressure and the gas fraction due to partitioning from the condensed phase. The second set of simulations includes also sea spray, in the form of sodium, chloride and sea-salt (ss) sulfate. For the concentrations of ss-sulfate and chloride we used the median values from ACE, whereas the sodium concentration was increased to achieve neutrality of the SSA and account for the presence of other cations which cannot be included in E-AIM (*i.e.* magnesium and calcium). Finally, for the third set we considered only 10% of the sea spray concentration, together with nss-sulfate, MSA and different concentrations of ammonium spanning an ammonium to nss-sulfate ratio from 0.25 to 2. Results are shown in the main text. Table S2 shows the concentrations of aerosol constituents used for each model run.

The predicted MSA gas phase concentrations shown in the main text (Fig. 8) was calculated considering the estimated gas phase fraction from each E-AIM simulation multiplied by the average particulate MSA concentration measured during the two periods under analysis (0.21 μg m^{-3} and 0.09 μg m^{-3} for the first and the second period, respectively).

References

Barnes, I., Hjorth, J., & Mihalapoulos, N. (2006). Dimethyl sulfide and dimethyl sulfoxide and their oxidation in the atmosphere. *Chemical Reviews*, *106*(3), 940–975. doi: https://doi.org/10.1021/cr020529+

Clarke, J. H. R., & Woodward, L. A. (1966). Raman spectrophotometric determination

of the degrees of dissociation of methanesulphonic acid in aqueous solution at 25°C. *Trans. Faraday Soc.*, *62*, 2226–2233. doi: 10.1039/TF9666202226

Clegg, S., & Brimblecombe, P. (1985). The solubility of methanesulphonic acid and its implications for atmospheric chemistry. *Environmental Technology Letters*, *6*(1-11), 269–278. doi: 10.1080/09593338509384344

Clegg, S. L., & Seinfeld, J. H. (2006). Thermodynamic Models of Aqueous Solutions Containing Inorganic Electrolytes and Dicarboxylic Acids at 298.15 K. 1. The Acids as Nondissociating Components. *The Journal of Physical Chemistry A*, *110*(17), 5692–5717. doi: 10.1021/jp056149k

Dal Maso, M., Kulmala, M., Lehtinen, K. E., Mäkelä, J., Aalto, P., & O'Dowd, C. (2002). Condensation and coagulation sinks and formation of nucleation mode particles in coastal and boreal forest boundary layers. *Journal of Geophysical Research*, *107*(D19), 8097. doi: 10.1029/2001JD001053

De Bruyn, W. J., Shorter, J. A., Davidovits, P., Worsnop, D. R., Zahniser, M. S., & Kolb, C. E. (1994). Uptake of gas phase sulfur species methanesulfonic acid, dimethylsulfoxide, and dimethyl sulfone by aqueous surfaces. *Journal of Geophysical Research*, *99*(D8), 16927. doi: 10.1029/94JD00684

Dutcher, C. S., Wexler, A. S., & Clegg, S. L. (2010). Surface Tensions of Inorganic Multicomponent Aqueous Electrolyte Solutions and Melts. *The Journal of Physical Chemistry A*, *114*(46), 12216–12230. doi: 10.1021/jp105191z

Eisele, F. L., & Tanner, D. J. (1993). Measurement of the gas phase concentration of H2SO4and methane sulfonic acid and estimates of H2SO4production and loss in the atmosphere. *Journal of Geophysical Research*, *98*(D5), 9001–9010. doi: 10.1029/

93JD00031

Jokinen, T., Sipilä, M., Junninen, H., Ehn, M., Lönn, G., Hakala, J., ... Worsnop, D. R. (2012). Atmospheric sulphuric acid and neutral cluster measurements using CI-APi-TOF. *Atmospheric Chemistry and Physics*, *12*(9), 4117–4125. doi: 10.5194/acp-12-4117-2012

Kramp, F., & Paulson, S. E. (1998). On the uncertainties in the rate coefficients for OH reactions with hydrocarbons, and the rate coefficients of the 1,3,5-trimethylbenzene and m-xylene reactions with OH radicals in the gas phase. *Journal of Physical Chemistry A*, *102*(16), 2685–2690. doi: 10.1021/jp973289o

Myhre, C. E. L., D'Anna, B., Nicolaisen, F. M., & Nielsen, C. J. (2004). Properties of aqueous methanesulfonic acid: complex index of refraction and surface tension. *Applied Optics*, *43*(12), 2500. doi: 10.1364/AO.43.002500

Paulsen, D., Dommen, J., Kalberer, M., Prévôt, A. S. H., Richter, R., Sax, M., ... Baltensperger, U. (2005). Secondary Organic Aerosol Formation by Irradiation of 1,3,5-Trimethylbenzene-NO x -H 2 O in a New Reaction Chamber for Atmospheric Chemistry and Physics. *Environmental Science & Technology*, *39*(8), 2668–2678. doi: 10.1021/es0489137

Schmale, J., Baccarini, A., Thurnherr, I., Henning, S., Efraim, A., Regayre, L., ... Carslaw, K. S. (2019). Overview of the antarctic circumnavigation expedition: Study of preindustrial-like aerosols and their climate effects (ACE-SPACE). *Bulletin of the American Meteorological Society*, *100*(11), 2260–2283. doi: 10.1175/BAMS-D-18-0187.1

Sipilä, M., Sarnela, N., Jokinen, T., Henschel, H., Junninen, H., Kontkanen, J., ...

O'Dowd, C. (2016). Molecular-scale evidence of aerosol particle formation via sequential addition of HIO_3. *Nature*, *537*(7621), 532–534. doi: 10.1038/nature19314

Wine, P. H., Thompson, R. J., Ravishankara, A. R., Semmes, D. H., Gump, C. A., Torabi, A., & Nicovich, J. M. (1984). Kinetics of the reaction $OH + SO_2 + M \longrightarrow HOSO_2 + M$. Temperature and pressure dependence in the fall-off region. *The Journal of Physical Chemistry*, *88*(10), 2095–2104. doi: 10.1021/j150654a031

Figures

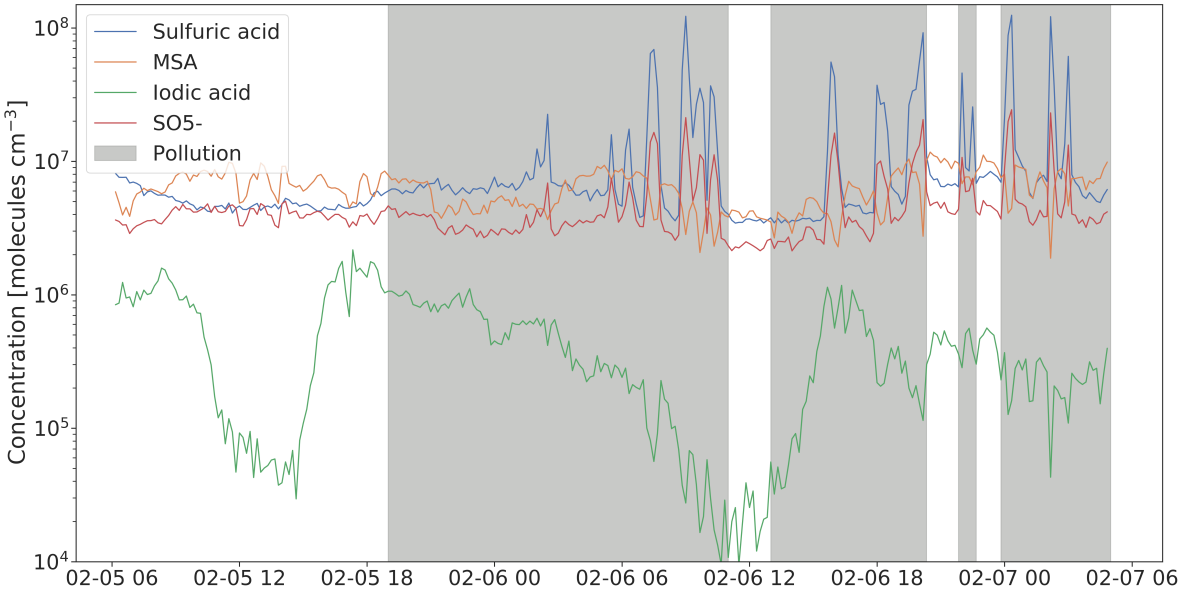

Figure S1. Time series showing the effect of pollution on the major compounds measured with the nitrate CI-APi-ToF, the polluted periods are highlighted with a gray shadow according to the pollution mask described in Schmale et al. (2019). SO_5^- is generated inside the inlet of the CI-APi-ToF and is a proxy for ambient SO_2.

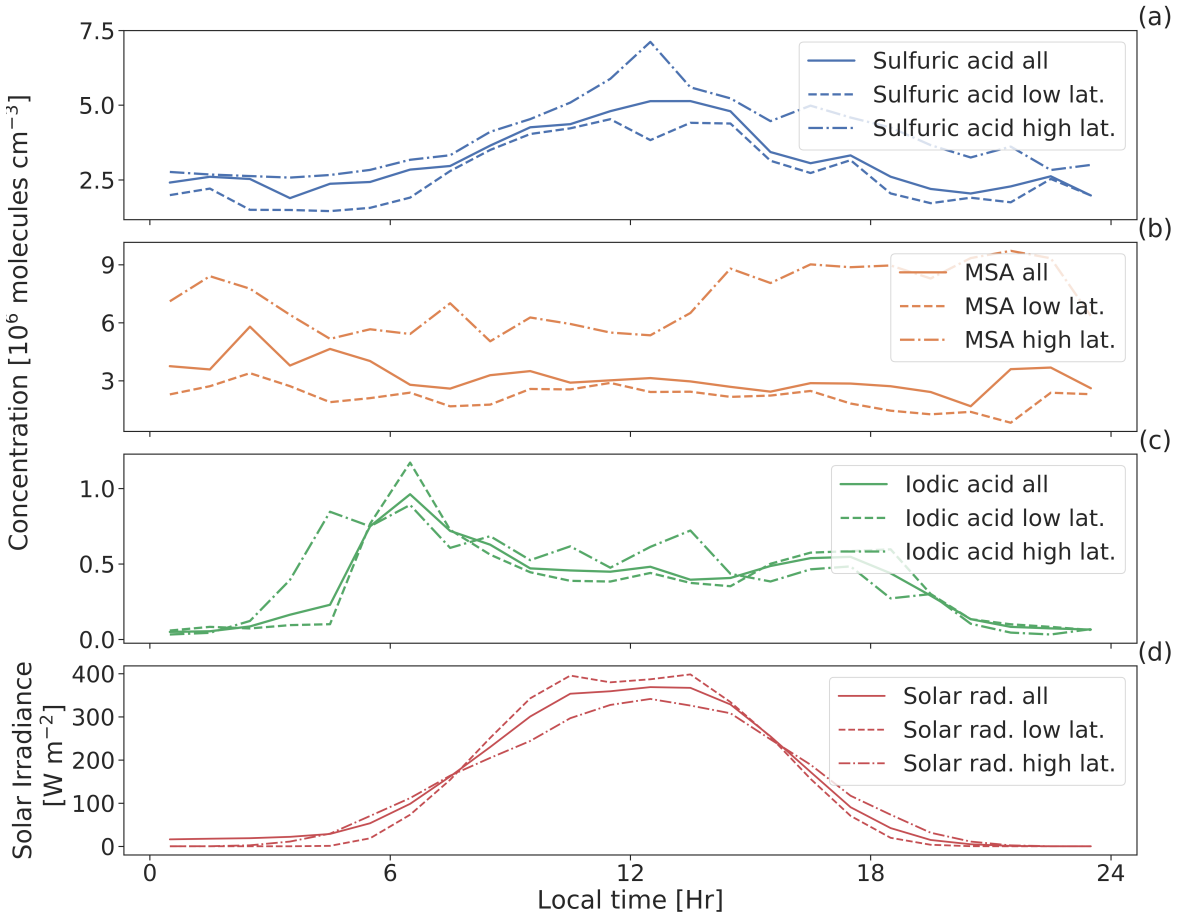

Figure S2. Diurnal profiles of **(a)** sulfuric acid, **(b)** MSA, **(c)** iodic acid and **(d)** solar irradiance for the entire campaign and separated by latitude. Here, high and low latitude indicates measurements above and below 60 °S, respectively.

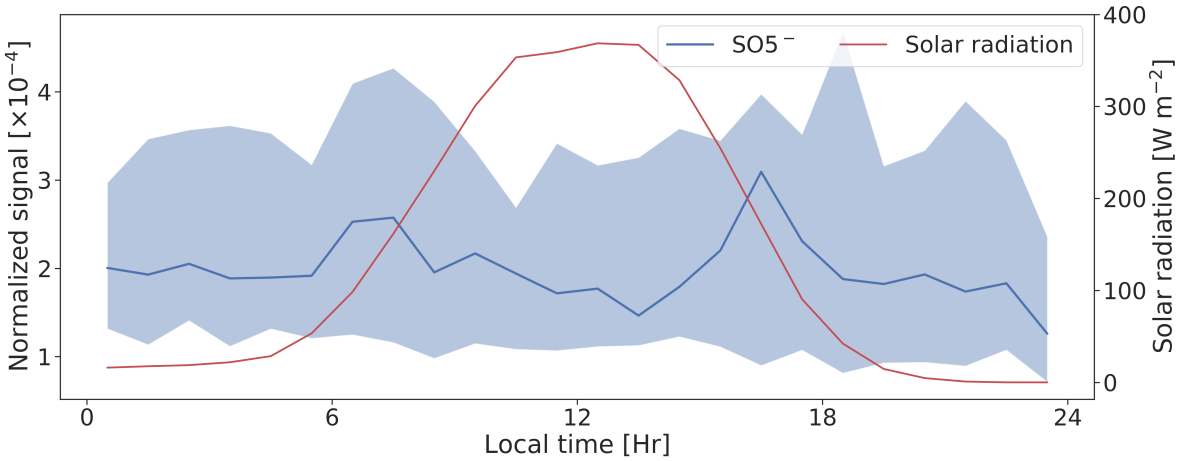

Figure S3. Diurnal cycle of SO_5^-. The thick line represents the median and the shaded area the interquartile range. The red line shows the solar irradiance median with values on the right axis.

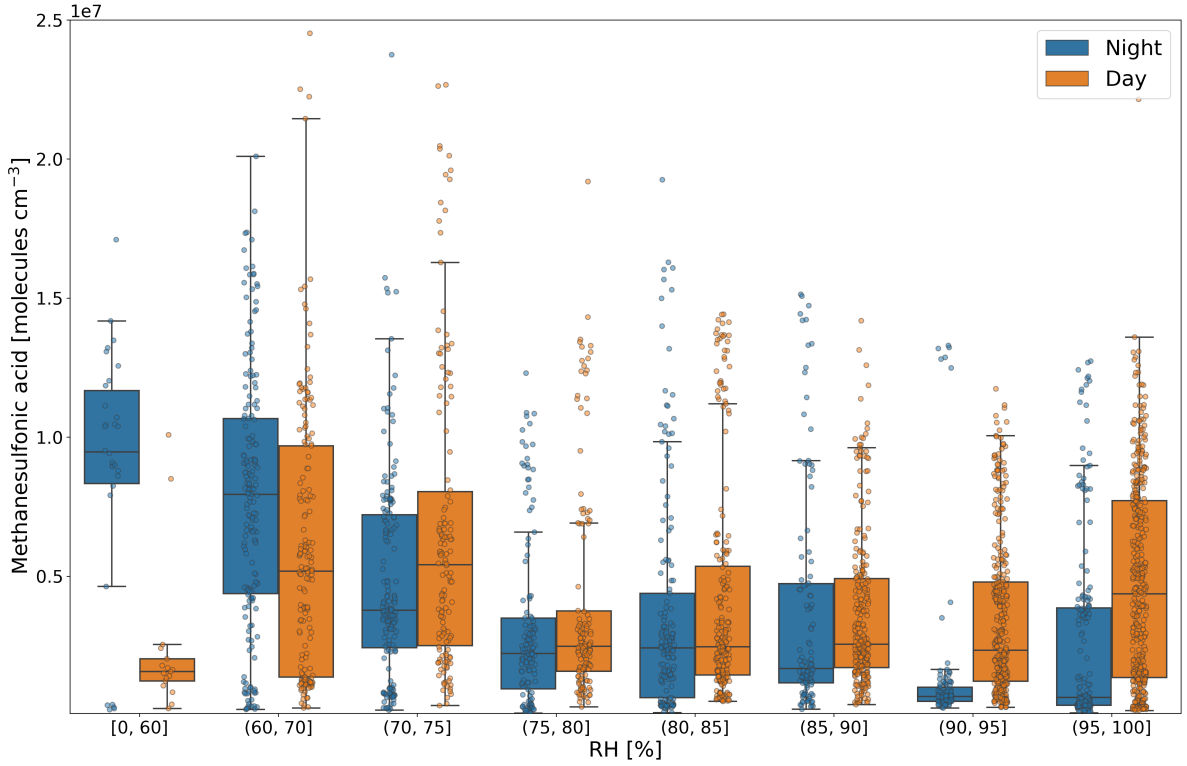

Figure S4. Gaseous MSA box and whiskers plot as a function of relative humidity (RH). Data were separated between day and night and binned into different RH classes as indicated by the axis label. The original data are shown with the small semi-transparent circles. The box extends from the first quartile (Q1) to the third quartile (Q3) with a line indicating the median. The whiskers are set to 1.5×[Q3-Q1].

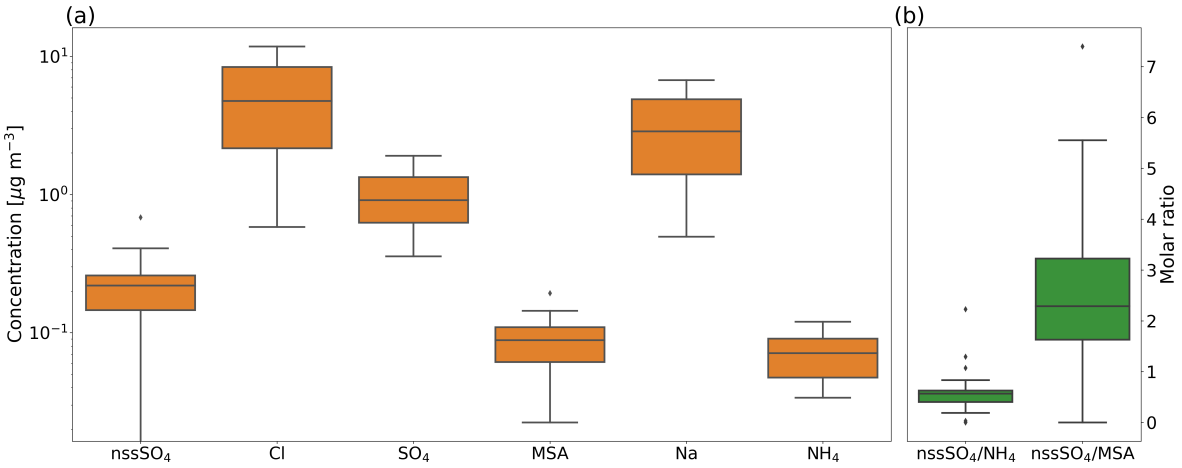

Figure S5. Box and whiskers plot of the ion chromatography data from PM_{10} daily aerosol filter. Only a subset of filters with minimum contamination from the ship exhaust was selected. (a) Concentration of the ions used for the thermodynamic modelling, (b) molar ratio of non-sea-salt (nss) sulfate to ammonium and nss-sulfate to MSA.

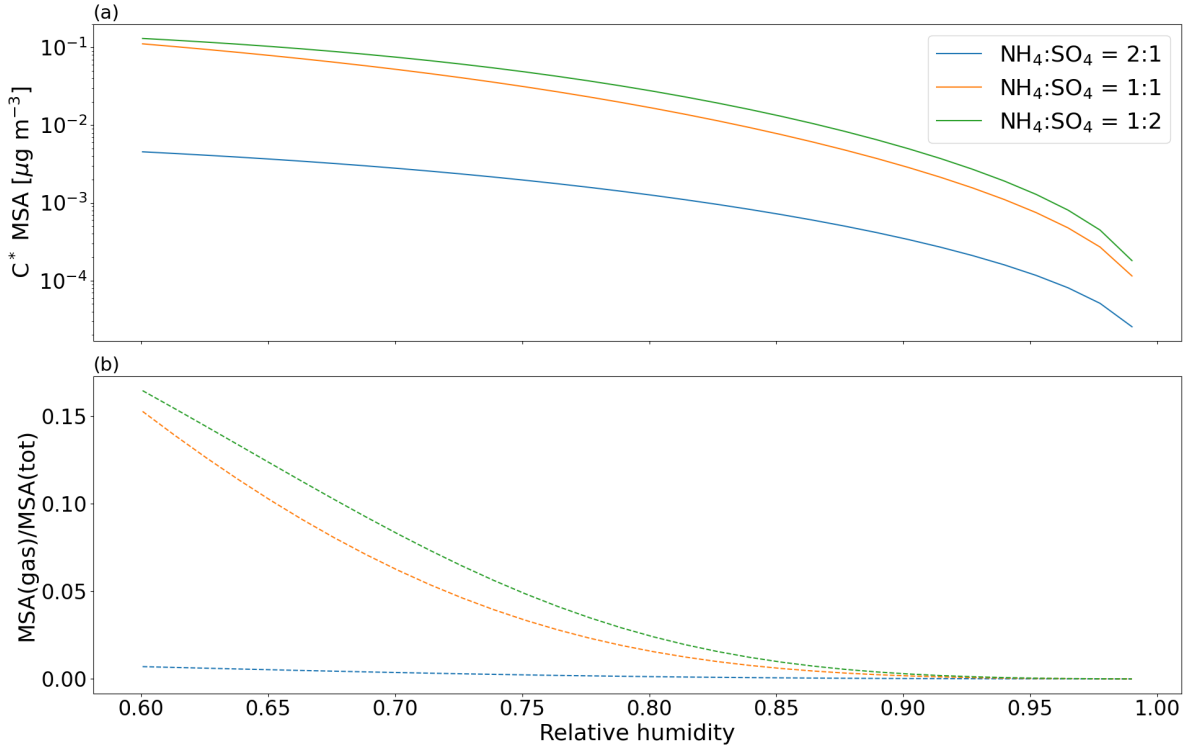

Figure S6. E-AIM results for MSA partitioning over an aerosol mixture composed of sulfate, MSA and ammonium as a function of relative humidity. **(a)** MSA equilibrium vapour pressure (C*), **(b)** fraction of MSA in the gas phase due to partitioning from the condensed phase. The sulfate, MSA and ammonium concentrations used for this simulation are reported in table S2 (run 1.1, 1.2 and 1.3).

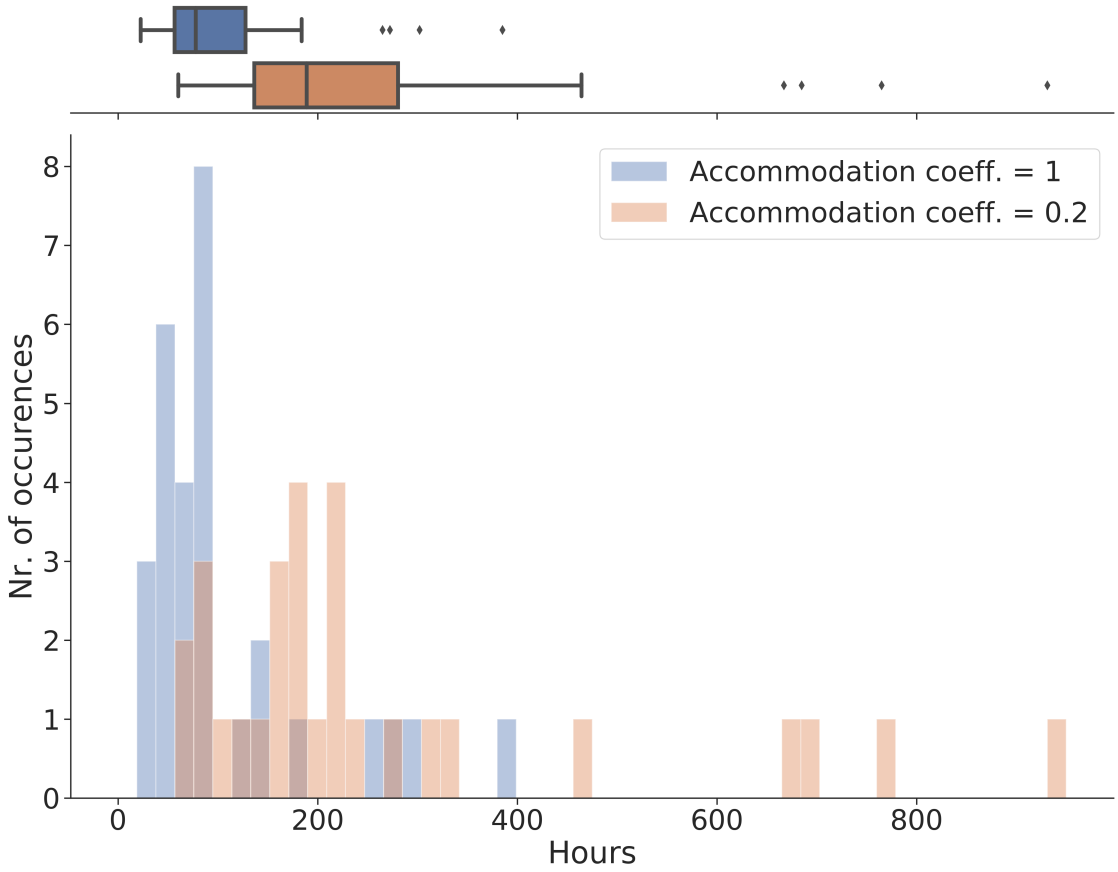

Figure S7. Number of hours required to reproduce the observed particulate MSA concentration assuming kinetic condensation of gaseous MSA with two different accommodation coefficients. This condensation time was calculated based on the daily average values and the figure shows the number of occurrences as a histogram and a box and whiskers plot on top. The box extends from the first quartile (Q1) to the third quartile (Q3) with a line indicating the median. The whiskers are set to 1.5×[Q3-Q1].

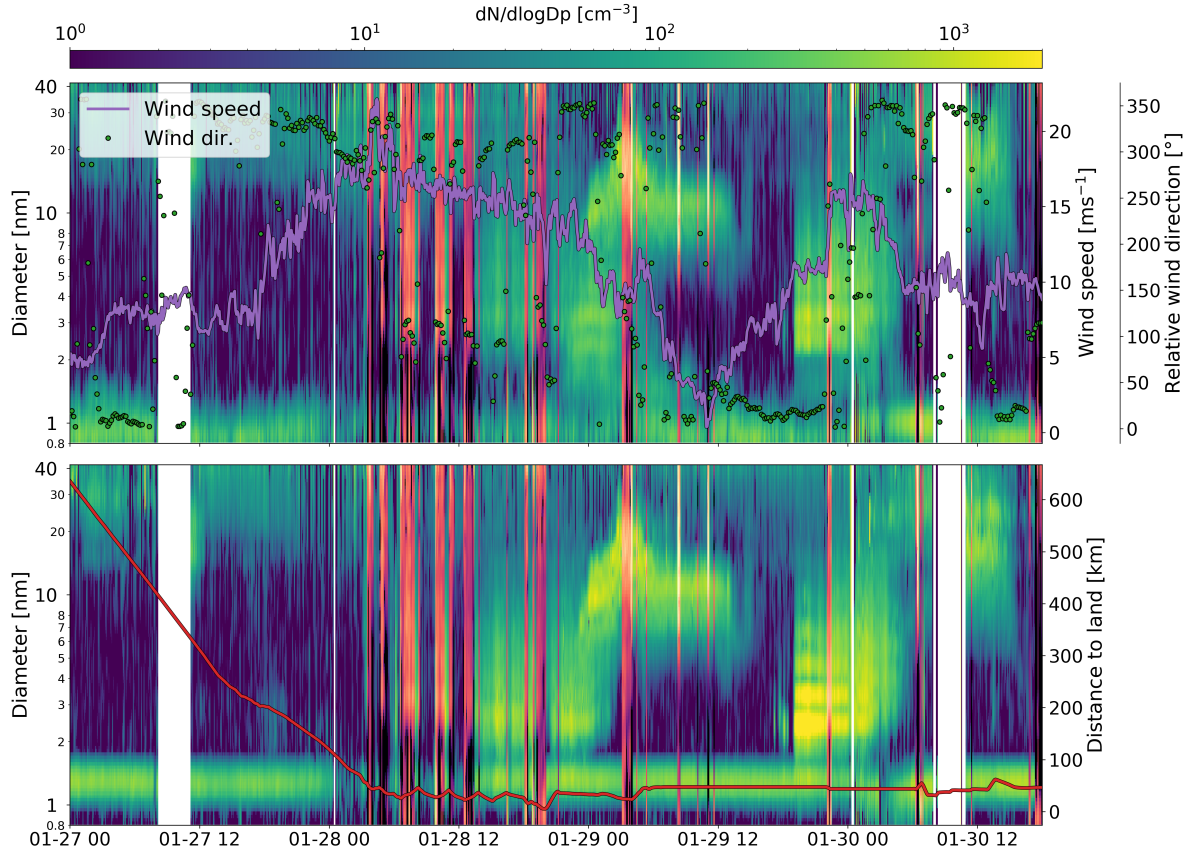

Figure S8. Wind induced ions, **(a)** negative ion size distribution and, on the right axis, wind speed and relative wind direction (the bow of the ship corresponds equivalently to 0° or 360°). **(b)** positive ion size distribution, on the right axis the distance to land is shown. Pollution periods are highlighted with a different color map (*magma*).

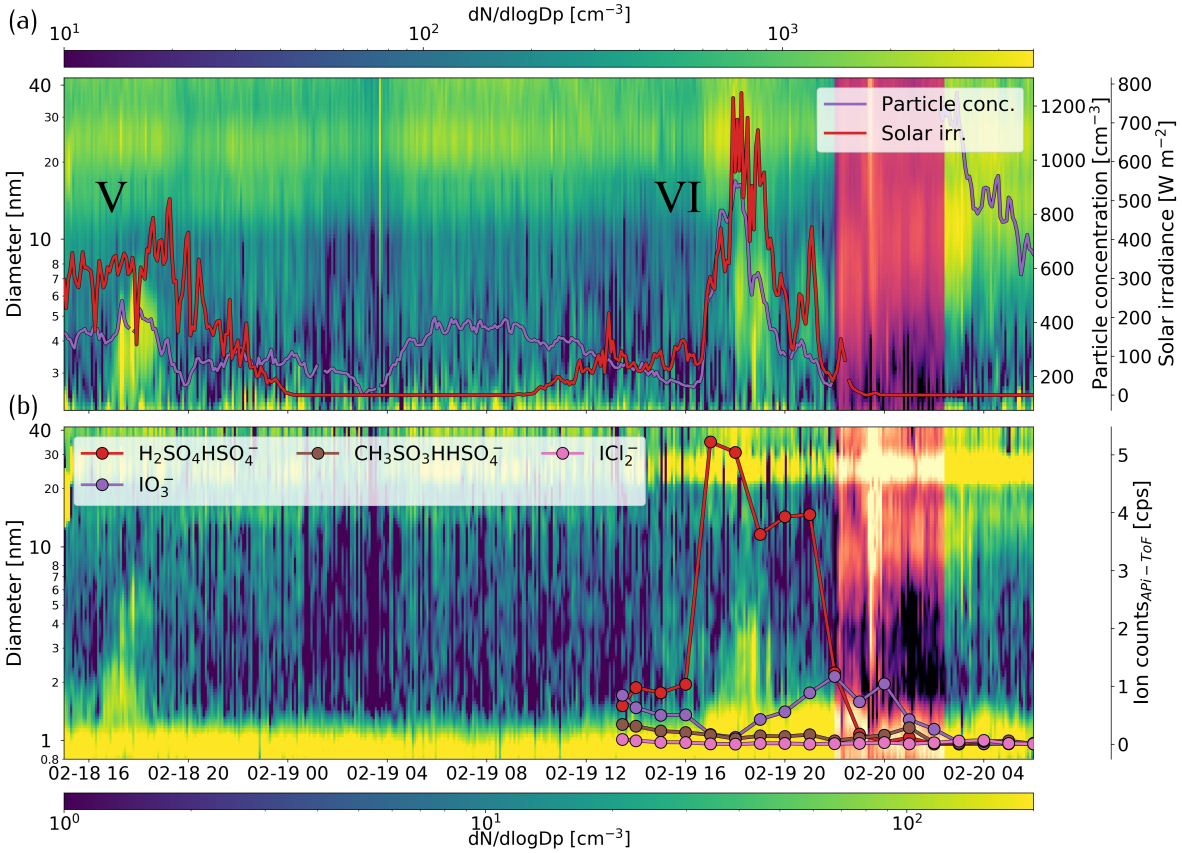

Figure S9. New particle formation event, **(a)** total particle size distribution and, on the right axis, number concentration of particles larger than 7 nm and solar irradiance time series. **(b)** negatively charged ion size distribution, on the right axis the concentration of negative ions measured with the APi-ToF (round markers) is reported. Only the 4 ions with the largest signal are reported here, the sulfuric acid and MSA monomers are not presented because of the instrument mass transmission, which was set to higher masses. Pollution spikes are highlighted with a different color map (*magma*).

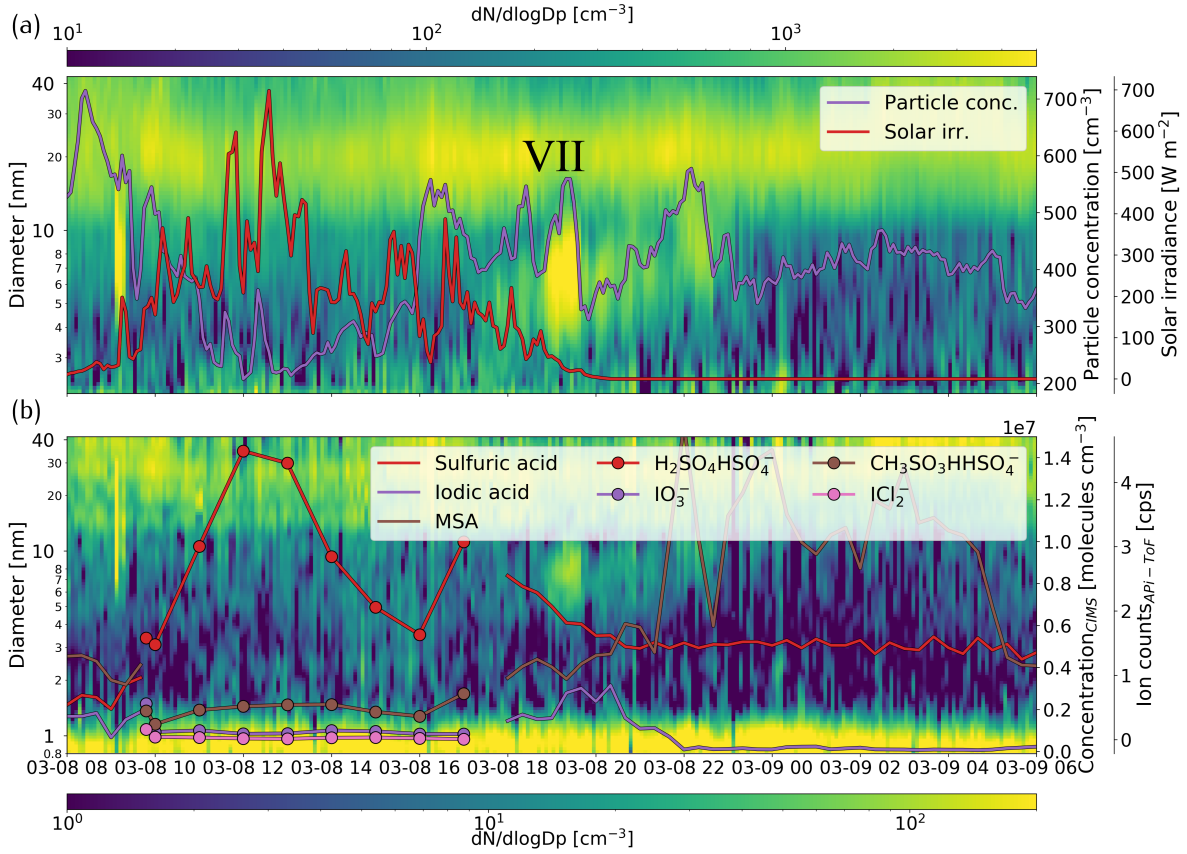

Figure S10. New particle formation event, **(a)** total particle size distribution and, on the right axis, number concentration of particles larger than 7 nm and solar irradiance time series. **(b)** negatively charged ion size distribution, on the right axis the concentration of neutral molecules measured with the CIMS (solid line) and the negative ions measured with the APi-ToF (round markers) are reported. Only the 4 ions with the largest signal are reported here, the sulfuric acid and MSA monomers are not presented because of the instrument mass transmission, which was set to higher masses.

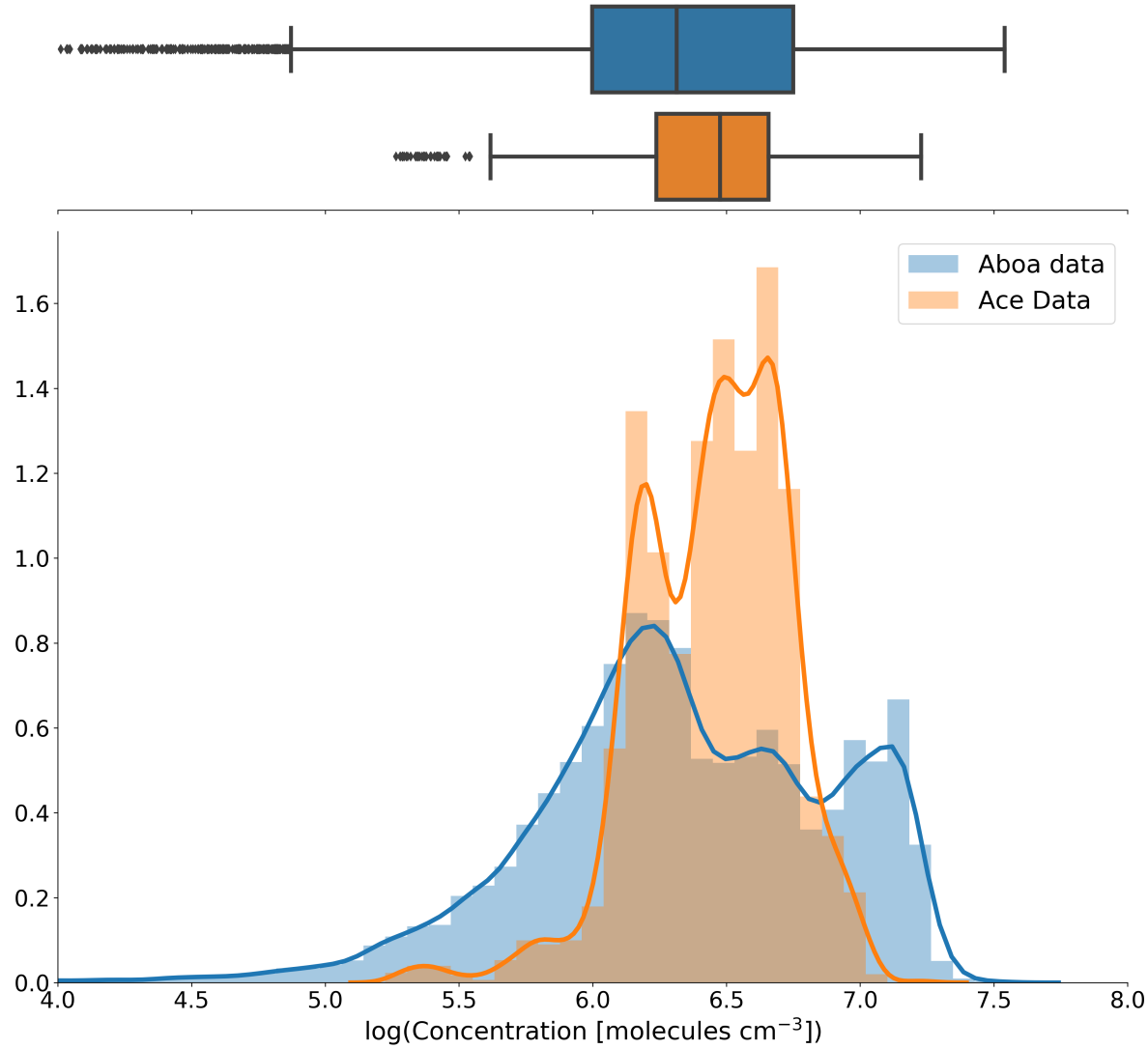

Figure S11. Comparison of the sulfuric acid measured during ACE and at Aboa. The figure shows a histogram reporting the frequency of the observation with a kernel density estimate (thick line) and box and whiskers plot on top. The box extends from the first quartile (Q1) to the third quartile (Q3) with a line indicating the median. The whiskers are set to 1.5×[Q3-Q1].

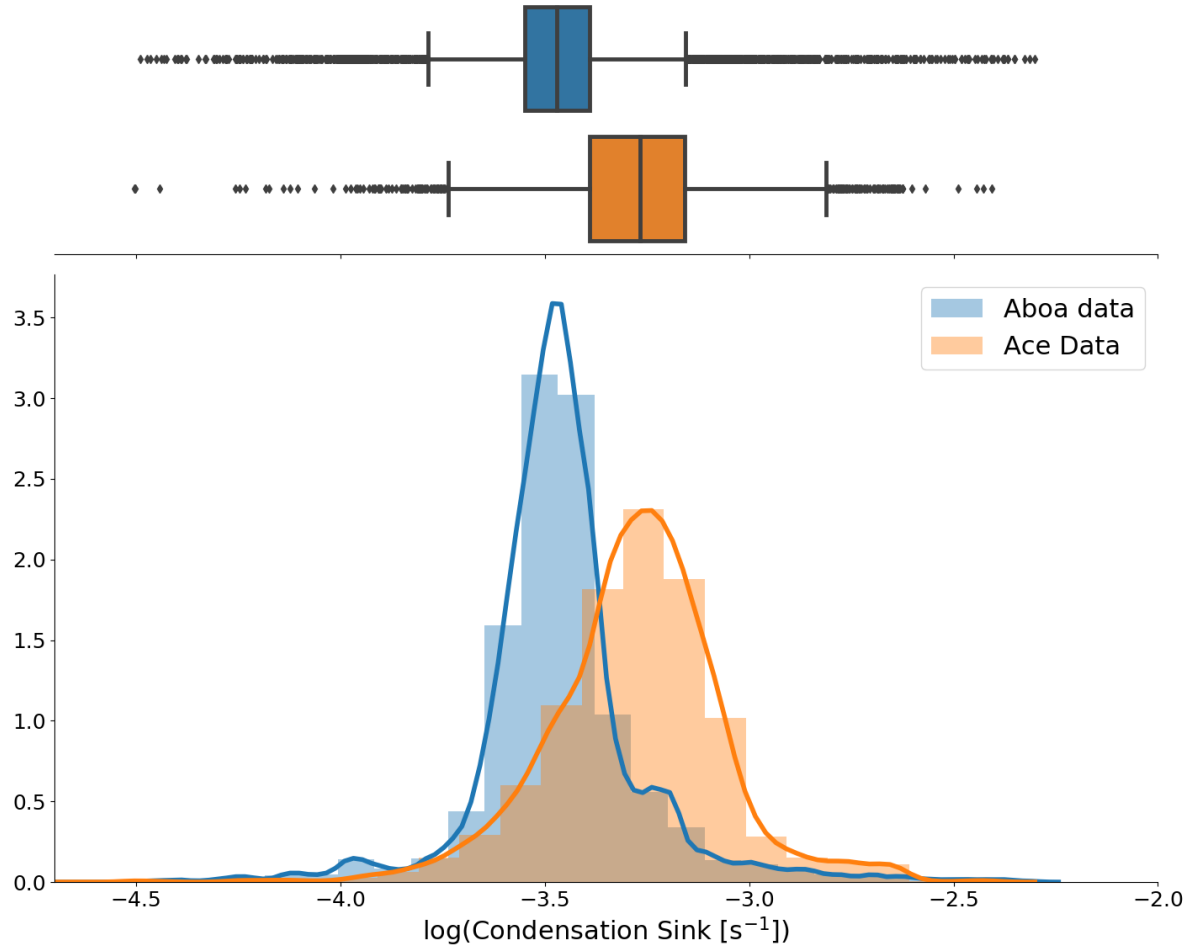

Figure S12. Comparison of the condensation sink measured during ACE and at Aboa. The figure shows a histogram reporting the frequency of the observation with a kernel density estimate (thick line) and box and whiskers plot on top. In this case the condensation sink from ACE was calculated using the same size range as at Aboa to improve the accuracy of the comparison (from 10 nm to 900 nm). The box extends from the first quartile (Q1) to the third quartile (Q3) with a line indicating the median. The whiskers are set to 1.5×[Q3-Q1].

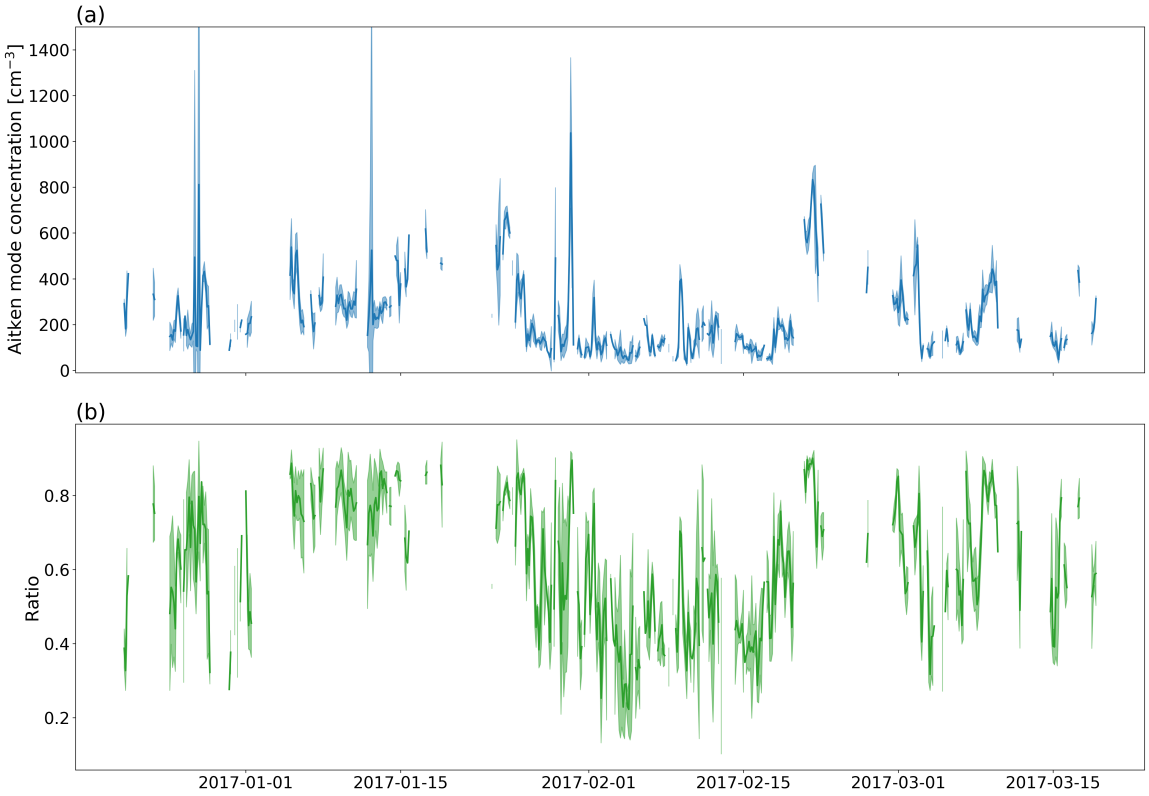

Figure S13. Aitken mode particles during ACE: **(a)** total Aitken mode particle number concentration from the fit of the SMPS size distribution and **(b)** ratio of the Aitken mode particle number to the total number particle concentration. The thick line is a 3 hours mean and the shadowed region indicates a 1 standard deviation interval.

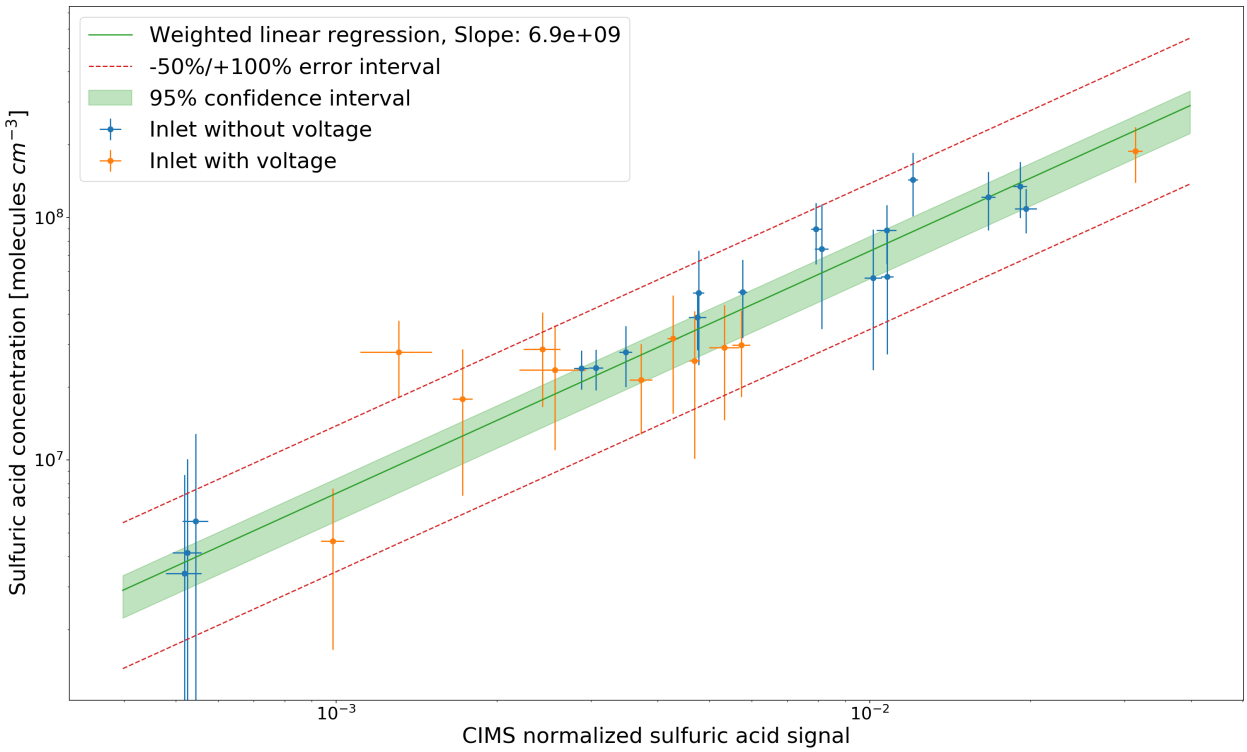

Figure S14. Sulfuric acid calibration with smog chamber experiments. Each data point represents a different experiment with the CI-APi-ToF normalized sulfuric acid signal on the x-axis and the corresponding concentration of sulfuric acid inside the chamber on the y-axis. Error bars on the x-axis are equal to the standard error of the mean whereas errors on the y-axis are equal to the propagated uncertainty via Equation 3. Orange and blue markers indicate measurements where the CI inlet was operated with and without voltage, respectively.

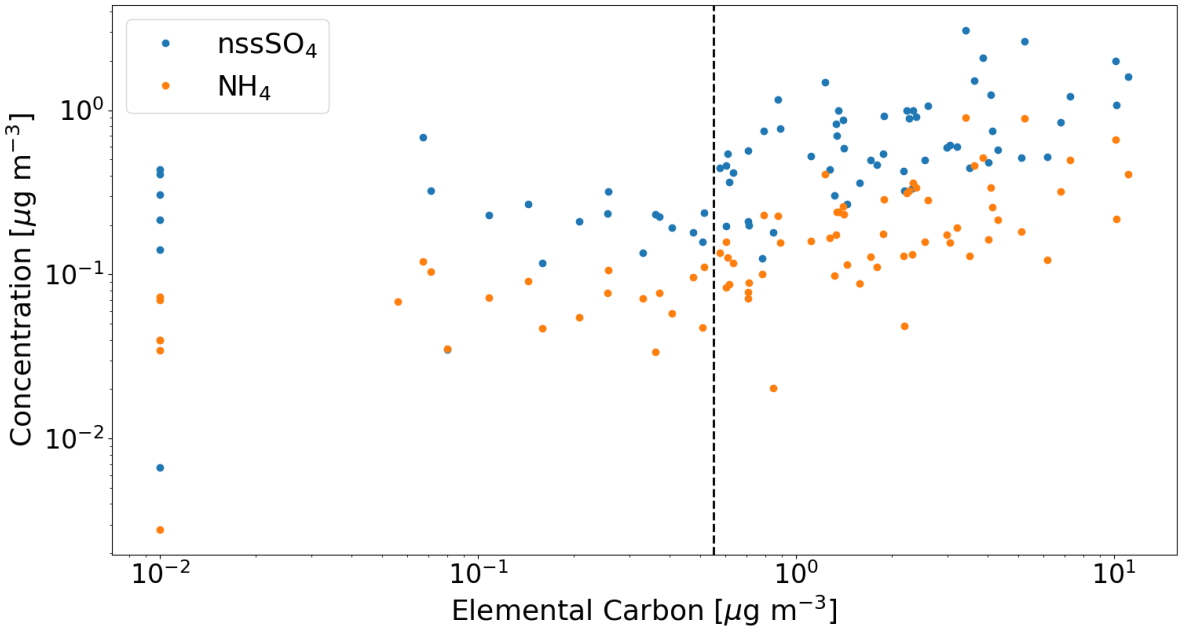

Figure S15. Concentration of nss-sulfate and ammonium as a function of elemental carbon. The vertical dashed line was drawn at 0.65 μg m^{-3} of carbon and indicates the concentration below which the effect of ship pollution is not evident anymore on nss-sulfate and ammonium. Elemental carbon measurements below detection limit were fixed to a value equal to 0.01 μg m^{-3}.

Tables

Table S1. MSA thermodynamic properties

Property	Unit of measure	Value	Reference
Molar mass	g mol^{-1}	96.1	Barnes et al. (2006)
Molar Volume	cm^3 mol^{-1}	64.93	Barnes et al. (2006)
First dissociation constant	mol kg^{-1}	73	Clarke and Woodward (1966)
Enthalpy of dissociation	kJ mol^{-1}	0	Not determined
Henry's law constant	mol kg^{-1} atm^{-1}	8.9×10^{11}	S. Clegg and Brimblecombe (1985)
Henry's law enthalpy change	kJ mol^{-1}	14.644	De Bruyn et al. (1994)
Surface tension: c_1	mN m^{-1}	138.23	Myhre et al. (2004)
Surface tension: c_2	mN m^{-1} K^{-1}	−0.284	Myhre et al. (2004)
Surface tension: a_{ws}	mN m^{-1}	147.86	Myhre et al. (2004)
Surface tension: b_{ws}	mN m^{-1} K^{-1}	−0.275	Myhre et al. (2004)
Surface tension: a_{sw}	mN m^{-1}	−167.117	Myhre et al. (2004)
Surface tension: a_{sw}	mN m^{-1} K^{-1}	0.400	Myhre et al. (2004)

Table S2. Concentration of aerosol constituents used for the E-AIM simulations

Run number	nss-sulfate nmol m^{-3}	Ammonium nmol m^{-3}	MSA nmol m^{-3}	ss sulfate nmol m^{-3}	Chloride nmol m^{-3}	Sodium nmol m^{-3}
1.1	2.3	4.6	1	0	0	0
1.2	2.3	2.3	1	0	0	0
1.3	2.3	1.15	1	0	0	0
2.1	2.3	3.9	1	7.2	134	148
3.1	2.3	4.6	1	0.7	13.4	14.8
3.2	2.3	2.3	1	0.7	13.4	14.8
3.3	2.3	1.15	1	0.7	13.4	14.8
3.4	2.3	0.58	1	0.7	13.4	14.8